Materials Research Proceedings 28 (2023) 65-74 https://doi.org/10.21741/9781644902479-8

Process-dependent material characteristics of DMLS-manufactured specimens

ZETTEL Dominic[1,2,a *], BREITKOPF Piotr[2,b], NICOLAY Pascal[1,c] and WILLMANN Roland[1,d]

[1]Carinthia University of Applied Sciences (CUAS), research group AMAViS[2] and CiSMAT Europastraße 4, 9524 Villach, Austria

[2]Université de Technologie de Compiègne (UTC), Laboratoire Roberval FR3272, CS 60319 60203 Compiègne Cedex, France

[a]d.zettel@cuas.at, [b]piotr.breitkopf@utc.fr, [c]p.nicolay@cuas.at, [d]r.willmann@cuas.at

Keywords: Direct Metal Laser Sintering, Strengthal, Thermal Conductivity, Microstructure

Abstract. Direct metal laser sintering is a 3D-printing technology involving a multitude of physical phenomena requiring the fine-tuning of multiple parameters (e.g., laser power, layer thickness) to achieve satisfying fabrication results [1]. Modifying each of these parameters can significantly influence the resulting material characteristics of the fabricated parts [2]. This work investigates the impact of the modification of the process parameters on the material characteristics of hardened aluminum specimens. A design of experiments was used to fabricate 85 aluminum specimens using 17 printing parameter sets. The specimens' dimensional accuracy, surface roughness, hardness, density, porosity, and thermal conductivity were investigated. Standardized, as well as self-designed test setups were used for this purpose. Furthermore, porosity measurements and microstructural investigations were performed using scanning electron microscopy and reflected light microscopy.

Introduction

Direct metal laser sintering (DMLS) is a well-known manufacturing technique that fabricates metallic structures following the layer-by-layer deposition principle. The metallic powder is selectively melted by a high-energy laser beam, following instructions from a 3D-CAD model (STL format). The solidification of tiny melt pools generated along the laser tracks create strong bonds between the different layers [3].

Due to the high process complexity of DMLS, every alloy requires tailor-made printing parameters ("standard parameter sets") to achieve maximum part density. Each parameter (e.g., hatch distance) can indeed influence one or several of the involved physical phenomena during printing (e.g., powder bed formation, fluid dynamics of the molten pool, solidification, residual stresses, heat absorption), resulting in strongly differing micro- and mesostructures [4]. It is also possible to modify these parameters to adjust the material characteristics of the fabricated structures (e.g., porosity). Furthermore, this can achieve parts with specific material characteristics (e.g., mechanical strength, thermal conductivity, damping capacity). However, to adjust the properties as desired, it is necessary to study all the involved phenomena, their mutual influence and their impact on the solidified micro- and mesostructure.

In this paper, we present the results of our work aimed at determining the influence of the main DMLS process parameters on the material properties of manufactured parts. We followed a design of experiments (DoE) methodology, and fabricated 85 specimens with 17 different sets of printing parameters (5 specimens per parameter set). The material characteristics (dimensional accuracy,

surface roughness, hardness, density, porosity, and thermal conductivity) were then investigated using professional and self-designed tools.

Method and Material

The process regarding the development, fabrication, and characterization of aluminum specimens with different material characteristics is schematically shown in Fig. 1.

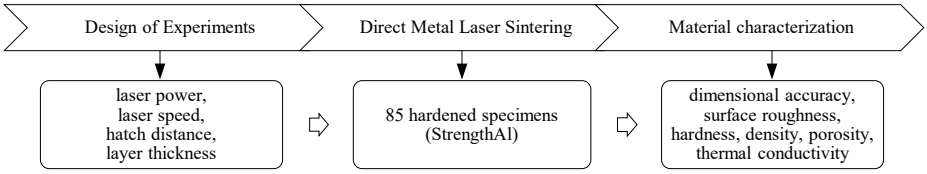

Fig. 1. Process for investigating the material characteristics of aluminium specimens fabricated with different printing parameter sets.

Design of Experiments. A DoE was performed, using the following variable parameters: laser power (P) [W], laser speed (v) [mm/s], hatch distance (h) [mm], and layer thickness (t) [mm]. The full factorial design (4 factors, 2 levels) results in 16 experiments with different energy densities (E) [J/mm³] given by:

$$E = \frac{P}{v \cdot h \cdot t} \quad (1)$$

To detect non-linear dependencies between factors, we added the "center point" experiment corresponding to the average values of parameters.

The specimens had the shape of rectangular solids (12*12*75 mm³), directly attached to the build platform without a support structure. Each printing parameter set from the DoE (17) was used five times. We, therefore, fabricated 85 specimens in total. The powder material is "StrengthAl" from the company m4p GmbH, a hardenable high-strength aluminum alloy consisting of Aluminum (main alloying element), Magnesium, Silicon, Scandium, Titanium, Zirconium, Manganese, and Chrome [5].

Direct Metal Laser Sintering. The fabrication of the specimens was executed with an EOS M290 printing system with a build volume of 250*250*325 mm³ and a 400 W Yb-fiber laser (spot size 100µm). A ceramic blade (hard recoating) was used for the powder recoating, and Argon as an inert gas. The platform temperature was set to 180°C. The exposure sequence of the specimens was directed against the gas flow to keep the concentration of impurities as low as possible. The "stripes" exposure pattern was used (stripe width 7 mm), and the rotation angle was set to 67°.

The specimens were hardened afterward (precipitation hardening – 6 hours, 350°C, slow cooling in the air). Machining (milling, turning) was then performed on the specimens to achieve proper test geometries.

Material characterization. One set of specimens (17 different printing parameter sets) was used for microstructural investigations and porosity measurements via scanning electron microscopy (SEM) (JSM-IT500 – JEOL) and reflected light microscopy (RLM) (Axio Imager.M2m – Zeiss). The specimens were embedded in cold embedding resin (CEM 1000 Blue Pulver) with subsequent grinding and polishing operations (Silicon Carbide paper – grain size P1200, diamond suspension – grain size 3 µm, Silicone Dioxide suspension – grain size 0.05µm). The metallographic specimens were then further treated with a Keller-Wilcox etchant.

The four remaining sets of specimens (4x17 specimens) were used to investigate the specimens' dimensional accuracy, surface roughness, hardness, density, porosity, and thermal conductivity. All tests were performed at room temperature (20°C).

Material Characteristics

Dimensional accuracy.

The dimensional inspection of the specimens (as-build) was executed using an outside micrometer (Micromar 40 ER – Mahr) with a resolution of 0.001mm. Both side lengths of the quadratic specimens were measured ten times (20 measurements per specimen). The dimensions as a function of the applied energy density are shown in Fig. 2.

There is quite a large dispersion in the measurement results (the standard deviation is high, for a given energy density, but there is also significant variability depending on the energy density: 11.906 – 12.433 mm). This phenomenon is at least partly due to the increase in the size of the melt pools when the energy density increases. Bigger melt pools also tend to aggregate more particles on the edges of the test specimens. It can be seen, however, that specimens fabricated with the same energy density but with different printing parameter sets (e.g., 112.23 J/mm³) show differences regarding their dimensions (red circles vs. black crosses).

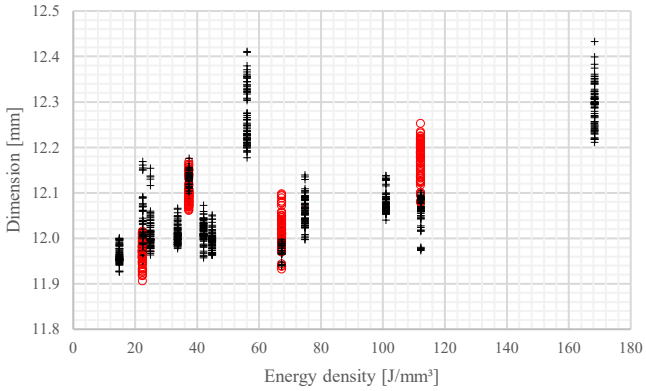

Fig. 2. Dimensional accuracy of printed specimens as a function of the applied energy density.

Surface roughness.

The surface roughness of the specimens (as-build) was measured using a perthometer (MarSurf GD25 – Mahr). Each side of every specimen was measured twice (8 measurements per specimen). The arithmetic average roughness (R_a), the average peak-to-valley profile roughness (R_z), and the maximum peak-to-valley profile height (R_{max}) as a function of the applied energy density are shown in Fig. 3.

The graph shows a correlation between the applied energy density and the surface roughness. The surface roughness slowly increases with the applied energy density, partly due to the increase of the size in the melt pools. Indeed, more particles adhere on the edges of bigger melt pools, which results in rougher surfaces. However, the energy density partly explains the observations. Specimens fabricated with the same energy density but with different printing parameter sets (e.g., 112.23 J/mm³) may not have the same surface roughness (red vs. black).

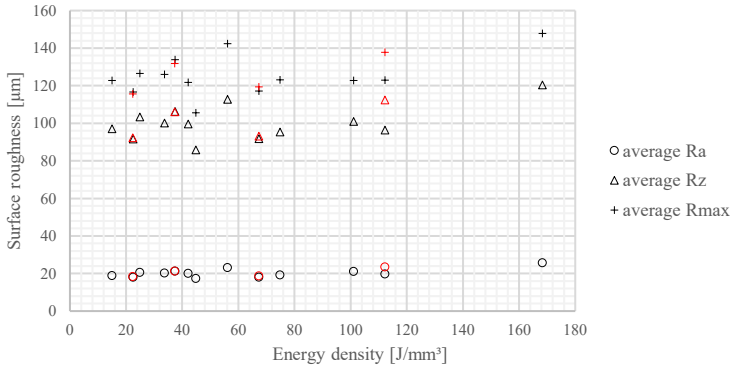

Fig. 3. Surface roughness of printed specimen as a function of the applied energy density.

Hardness.

The hardness testing of the specimens (milled) was performed using a universal hardness testing machine (ZHU 187.5 – ZwickRoell). Here, the Vickers hardness (HV) was measured using a diamond pyramid with an angle of 136° and a test force of 98.07 N. Each side of every specimen was measured twice (8 measurements per specimen). The HV as a function of the applied energy density is shown in Fig. 4.

The range of variation of the measurement results is extensive (46.2 – 163.1HV). The results show that the hardness increases to a certain energy (~70J/mm³). It then decreases again. This phenomenon is a consequence of the different printing parameter sets (different energy inputs) in combination with the subsequent hardening process. In the case of DMLS parts, hardening ("solution heat treatment") already occurs during the fabrication process when the melt pools quickly cool down. The second annealing step, called "aging treatment" still has to be performed afterward. Therefore, the solution heat treatment varies due to the different energy inputs of the printing parameter sets. Besides, specimens fabricated at lower energy densities show a more significant standard deviation in the measurement results than those fabricated at higher energy densities due to differences in the resulting porosity. The probability of hitting a (hidden) pore with the indenter is much higher in a porous material than in a more homogeneous one (the porosity increases when the energy density decreases, as shown later in this paper). It can also be seen that specimens fabricated with the same energy density but with different printing parameter sets (e.g., 112.23 J/mm³) show differences regarding their hardness (red circles vs. black crosses).

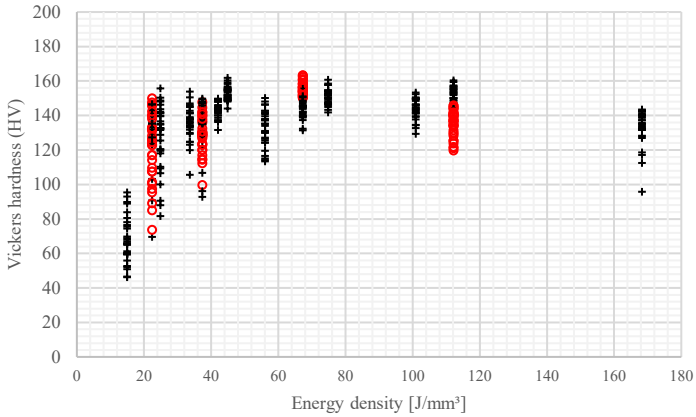

Fig. 4. Vickers hardness of printed specimens as a function of the applied energy density.

Density. The density (ρ) [g/cm³] of the specimens (milled) was determined according to:

$$\rho = \frac{m}{V} \quad (2)$$

where m [g] is the mass, and V [cm³] is the volume of the specimens. The specimens' weight was measured using a high-precision scale (AG204 DeltaRange - Mettler Toledo) with a resolution of 0.0001g. The specimens' volume was calculated using the dimensional inspection's measured volume. The density as a function of the applied energy density is shown in Fig. 5.

The range of variation of the measurement results is wide (2.21 - 2.65 g/cm³). The density significantly increases up to an energy density of about 30 J/mm³ and stays more or less constant above this point. There are no significant differences between specimens fabricated with the same energy density but different printing parameter sets (e.g., 22.45 J/mm³, red circles vs. black crosses).

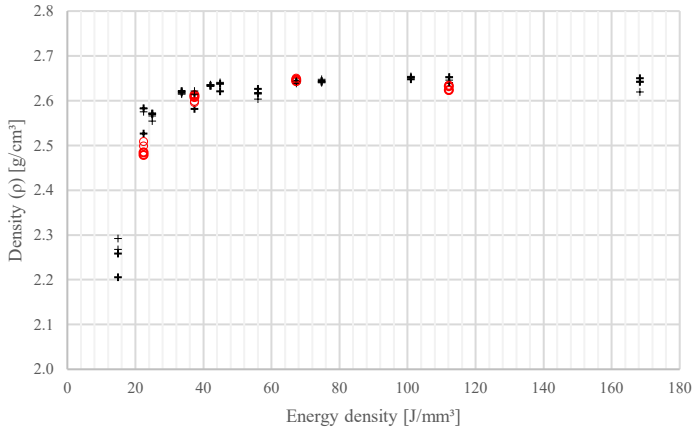

Fig. 5. Density of printed specimens as a function of the applied energy density.

Porosity and microstructure.

The porosity (pore size and pore size distribution) of the 17 metallographic specimens was measured using RLM and image processing software (ZEN core – Zeiss). The average total pore area in percent as a function of the applied energy density is shown in Fig. 6.

The range of variation of the measurement results is large (0.04 – 21.16%). The porosity significantly decreases for an energy density below 30 J/mm³. It stabilizes around 30 J/mm³ before slightly increasing for higher energy densities (>110 J/mm³). Specimens fabricated with the same energy density but with different printing parameter sets (e.g., 22.45 J/mm³) show differences regarding the average total pore area (red circles vs. black crosses).

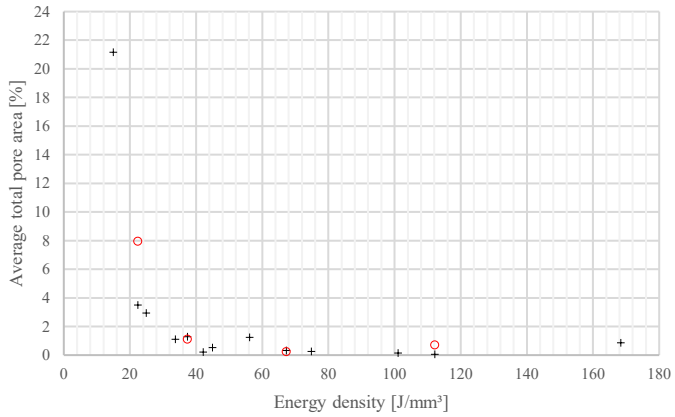

Fig. 6. Average total pore area of specimens as a function of the applied energy density.

The structure of the 17 metallographic specimens was further investigated using RLM and SEM. In this paper, we compare two specimens, the one with the lowest porosity (0.04%), and the one with the highest porosity (21.16%).

At first, the metallographic specimens (polished, not etched) were investigated using RLM, as shown in Fig. 7. Here, the different porosities are noticeable (Fig. 7, A vs. Fig. 7, B). A closer look at the porous structure (Fig. 7, B) shows that the pores are homogeneously distributed throughout the entire geometry. Due to irregular cooling rates (which depend on the build height and geometry of the printed part), DMLS parts can have an inhomogeneous microstructure with anisotropic material characteristics [6]. In our case however, the build height did not appear to influence the pore size and pore size distribution.

The metallographic specimens (polished, not etched) were further investigated using SEM, as shown in Fig. 8. Here, a magnification of 50 was used. The pictures clearly show the differences between the specimens regarding porosity. In the image of the porous structure (Fig. 8, B), fine powder particles that were not melted during the print job are still visible. There are significant differences in the size and shape of the pores. Also, note that the build direction cannot be detected from the pictures.

The metallographic specimens were etched to investigate them via RLM further, as shown in Fig. 9. Now, the typical laser beam tracks due to the layer-wise manufacturing principle of DMLS are visible. Fine powder particles are again apparent in Fig. 9, B. Splashes or inclusions could not be detected.

In addition, Energy Dispersive X-ray Spectroscopy (EDX) was used to investigate the distribution of alloy elements in three different specimens (porosities: 0.23%, 1.11%, and 21.16%). The results show that Aluminum (the main alloy element) and Magnesium are homogeneously distributed, also around pores. The remaining alloy elements (Silicon, Scandium, Titanium, Zirconium, Manganese, and Chrome) could not be detected due to the detection limit of the EDX apparatus (0.2% by mass) (JSM-IT500 – JEOL).

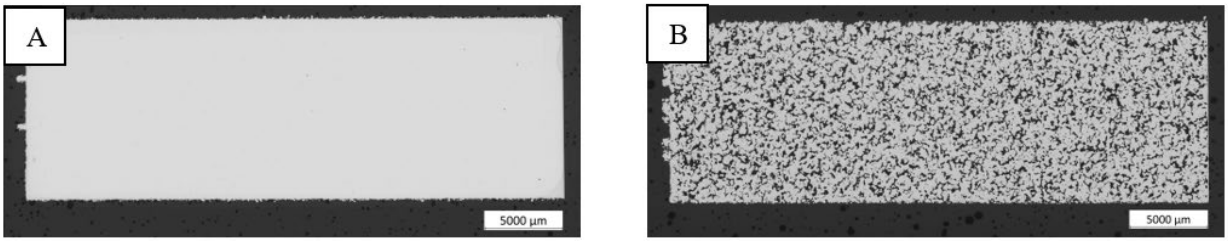

Fig. 7. RLM images of metallographic specimens showing different porosities (polished, not etched). A: dense structure fabricated with 112.23 J/mm³. B: porous structure fabricated with 14.96 J/mm³.

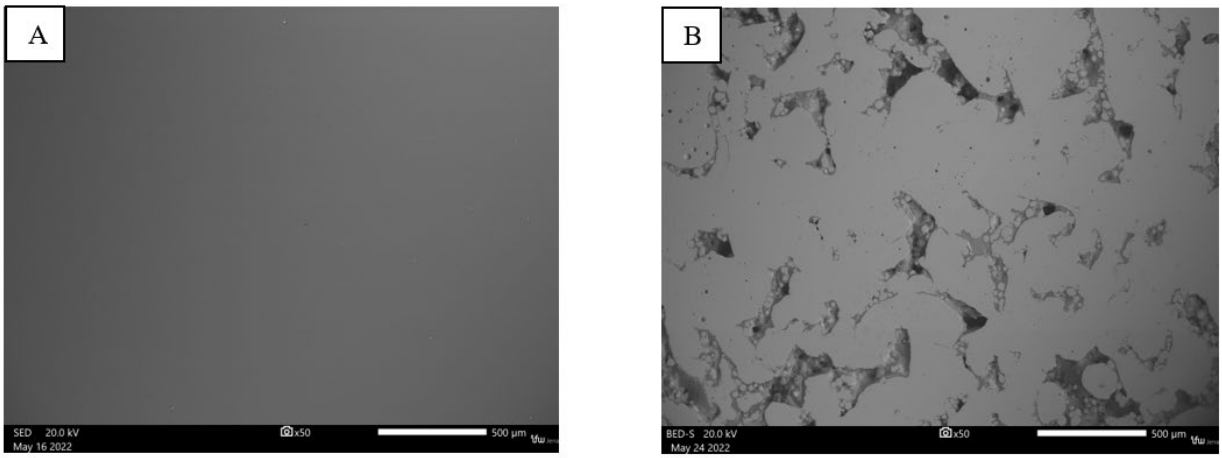

Fig. 8. SEM images of metallographic specimens showing different porosities (polished, not etched, magnification 50x). A: dense structure fabricated with 112.23 J/mm³. B: porous structure fabricated with 14.96 J/mm³.

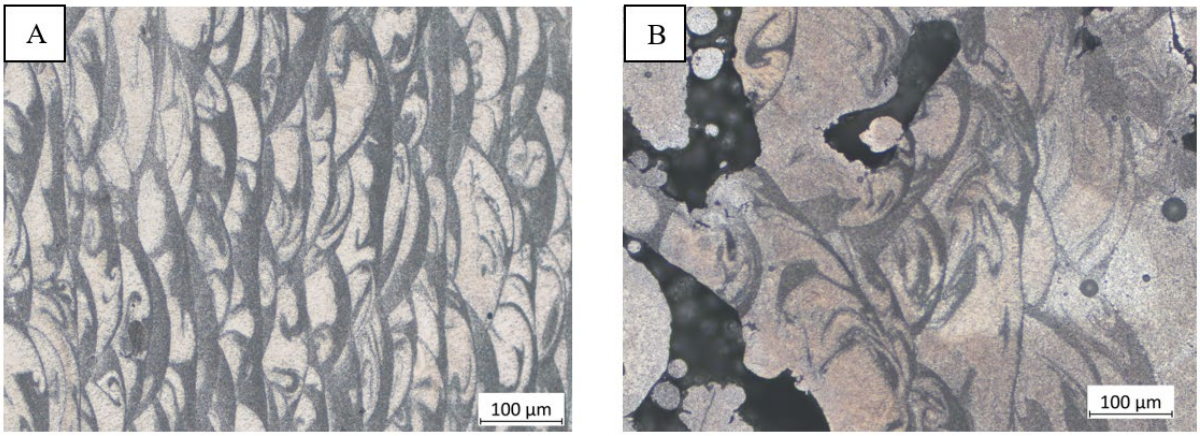

Fig. 9. RLM images of metallographic specimens showing different porosities (polished and etched). A: dense structure fabricated with 112.23 J/mm³. B: porous structure fabricated with 14.96 J/mm³.

Thermal conductivity. The specimens' thermal conductivity was measured using a self-designed test setup consisting of a hot plate (50°C) and a cold plate (0°C). On both plates, flux sensors are installed to measure the heat flux. PT1000 sensors are attached to each side of the specimens to measure the temperature gradient, as illustrated in Fig. 10.

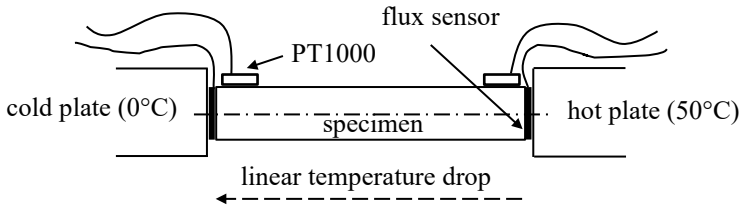

Fig. 10. Schematics of the self-designed test set-up used to measure the thermal conductivity of the fabricated samples.

The sensors are connected to an Arduino board, and digital tabletop multimeters are connected to a computer. The measured values are then used to calculate the thermal conductivity (λ) [W/mK] in Matlab (MathWorks) using:

$$\lambda = \frac{\phi \cdot x}{\Delta T \cdot A} \tag{3}$$

The heat flow (Φ) is obtained by:

$$\phi = \frac{Q}{t} \tag{4}$$

where (Q) [J] is the heat flux, t [s] is the time, x [m] is the length of the specimen, ΔT [K] is the temperature gradient between the two PT1000 sensors, and A [m^2] is the surface area of the specimen extremities in direct contact with the flux sensors.

We verified the validity of the measurements using a series of reference measurements using a known material with a thermal conductivity of 180 W/mK. All measurement results were located between 189.5 W/mK (5,3%) and 95.6 W/mK (4.4%). The average value for all 20 measurements was 179.02 W/mK.

Every printed specimen was measured five times. The measurement time was 180s. Fig. 11 and 12 show the thermal conductivity as a function of the applied energy density and the porosity.

Fig. 11 shows a wide range of variations in the measurement results (48.78-112.39 W/mK), probably due to substantial porosity variations between the different specimens, as shown in Fig. 12.

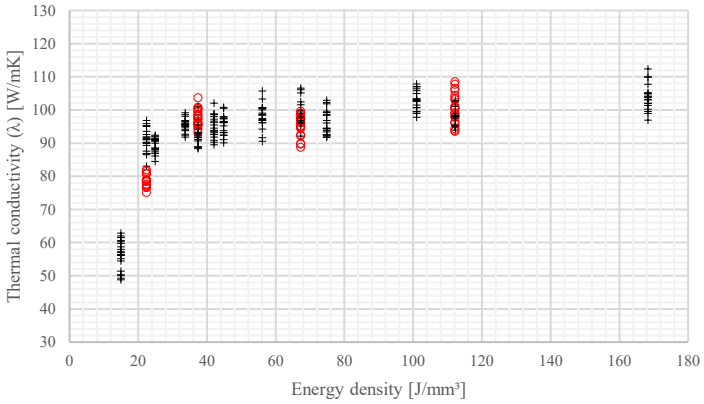

Fig. 11. Thermal conductivity of printed specimens as a function of the applied energy density.

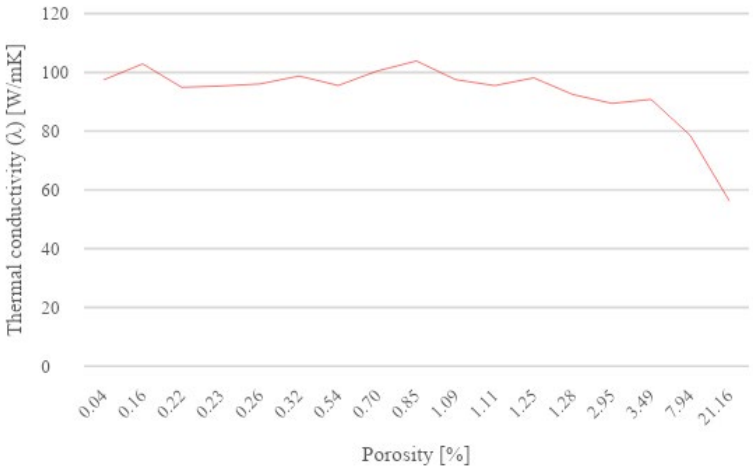

Fig. 12. Thermal conductivity of printed specimens as a function of the porosity.

Summary

An EOS M290 printing system was used to fabricate 85 aluminum specimens (StrengthAl) with 17 printing parameter sets, following a DoE approach (5x17 specimens). The modified printing parameters are the laser power (P) [W], laser speed (v) [mm/s], hatch distance (h) [mm], and layer thickness (t) [mm]. The specimens were then hardened (precipitation hardening) for 6 hours at 350°C with slow cooling in air. The specimens' dimensional accuracy, surface roughness, hardness, density, porosity, and thermal conductivity were then measured using professional tools and a self-designed test setup. Microstructural investigations were also performed using RLM and SEM.

The results show that changes in the process parameters (P, v, h, t) strongly affect the material characteristics, and while some variations follow visible trends, the energy density alone does not fully explain them. The hardening process also has an influence. Further work is required to better understand the physical mechanisms active during the formation and solidification of the melt pool.

Acknowledgement

This work was conducted in the frame of research cooperation between the research group Additive Manufacturing in Agile Virtual Systems for Product Design and Production Process Design (AMAViS^2), the Carinthia Institute for Smart Materials (CiSMAT), and the Laboratoire ROBERVAL of the Université de Technologie de Compiègne (UTC). AMAViS^2 and CiSMAT belong to the Carinthia University of Applied Sciences (CUAS). The work was mainly funded by AMAViS^2.

References

[1] J. Oliveira, A. LaLonde, J. Ma, Processing parameters in laser powder bed fusion metal additive manufacturing, Mat. & Design 193 (2020) 1-12.
[2] B.S. Rao, T.B. Rao, Effect of process parameters on powder bed fusion maraging steel 300: a review, Lasers Manuf. Mater. 9 (2022) 338-375. https://doi.org/10.1007/s40516-022-00182-6
[3] M.N. Jahangir, M.A.H. Mamun, M.P. Sealy, A review of additive manufacturing, AIP Conf. Proc. 1980 (2018), https://aip.scitation.org/doi/abs/10.1063/1.5044305
[4] T. Moges, G. Ameta, P. Witherell, A review of model inaccuracy and parameter uncertainty in laser powder bed fusion models and simulations, J. Manuf. Sci. Eng. 141 (2019) 1-14. https://doi.org/10.1115/1.4042789

[5] m4p material solutions GmbH, "www.metals4printing.com," 2022. Available: https://www.metals4printing.com/wp-content/uploads/datasheets/eng/Al-Base/m4p_Datasheet StrengthAl_EN.pdf. (accessed 02 May 2022).
[6] Z. Çağatay Öter, Anisotropic Mechanical Behavior of Direct Metal Laser Sintering (DMLS) Parts 3rd International Porous and Powder Materials Symposium (2017), Turkey.